

Calibration of ^{57}Fe Mössbauer Spectrometer Parameters for Hyper-fine Interaction Analysis

Brittany Callin¹ and Bronwen Olson²

¹*Department of Physics, University of Colorado Boulder, Boulder, Colorado 80309, USA*

²*Department of Physics, University of Texas at Dallas, Richardson, Texas 75080, USA*

(Dated: July 26, 2023)

Mössbauer spectroscopy is used to probe the fine nuclear structures of isotopes of Mössbauer nuclei. A common isotope used in Mössbauer spectroscopy is ^{57}Fe due to its low energy γ -rays, abundance, and long nuclear lifetime. We setup, calibrated and acquired data using a Mössbauer setup equipped with a 25 mCi ^{57}Co source by optimizing the full width at half-maximum (FWHM) and resolution using a krypton gas proportional counter detector. We cross-checked the relationship between channels and velocity of the Mössbauer drive unit using various absorbers: $\alpha\text{-Fe}$, Fe_2O_3 , $^{57}\text{FeC}_2\text{O}_4 \cdot 2\text{H}_2\text{O}$, and $\text{K}_2\text{Mg}^{57}\text{Fe}(\text{CN})^6$. From the spectroscopy of each absorber we measured the absorption energies of the peaks and derived the isomer shift, quadrupole splitting, and magnetic dipole interactions for all of the absorbers.

I. INTRODUCTION

Mössbauer spectroscopy was discovered in 1958 by R.L. Mössbauer [1]. Before then, the Bohr model was used to describe atomic resonant fluorescence, in which an excited atom emits a photon. This photon can give a ground-level atom of the same element enough energy to transition to the same excited state, producing a photon in the visible range. Nuclear resonant fluorescence was predicted to be the same by Kuhn in 1929 [2]. However, it was quickly shown that nuclear resonant scattering did not behave similarly to atomic resonant fluorescence due to conservation of momentum. When a γ -ray is emitted by a free atom, the atom experiences a recoil in the opposite direction of the emitted γ -ray. The recoil takes away energy from the γ -ray, so the γ -ray cannot be absorbed by a similar atom to the same excited state [2].

If a free atom is assumed to be stationary, the energy distribution of an excited state of the atom is centered around the energy difference between the excited state and the ground state. These energies are shifted in different directions by the recoil energy for emission and absorption peaks as shown in Fig. 1 [2]. The width at half height (FWHM) is approximately the natural width of the excited state. Free atoms cannot be assumed to be at rest due to thermal motion [2] that creates Doppler broadening. Doppler broadening widens absorption and emission peaks and creates overlap for the emission and absorption peaks which allows some resonant absorption to occur [3]. This broadening and overlap is sketched in Fig. 1. Mössbauer spectroscopy experiments tried to take advantage of this overlap by increasing the overlap by putting a radioactive source on a moving system to give incoming γ -rays more energy through the Doppler

effect, but these experiments were severely limited [2].

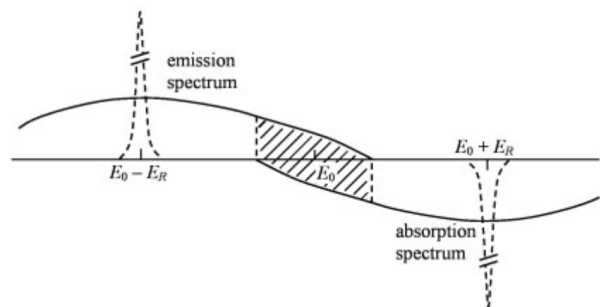


FIG. 1. *Energy spectrum for a free atom. Dashed line peaks represent emission and absorption peaks with no thermal motion and have a width at half height approximately equal to the natural width of the excited state. The solid lines show the energy spectrum of free atoms with thermal motion. The region with lines show the overlap of emissions and absorption spectrum that allows resonant absorption. Image sourced from Y.L. Chen and D.P. Yang [2].*

Mössbauer discovered that when an atom is bound in a crystal lattice the recoil will be absorbed into the atom's surrounding bonds. Recoil is minimized when the recoil energy is smaller than the energy of the chemical bonds keeping the atom bonded to other atoms [2]. The recoil mass, M , becomes the mass of the entire lattice. The recoil energy, E_R , is related to the mass by Eq. 1.

$$E_R = \frac{E_\gamma^2}{2Mc^2} \quad (1)$$

E_γ is the energy of the emitted γ -ray, and c is the speed of light [2]. From Eq. 1 it can be seen that recoil energy

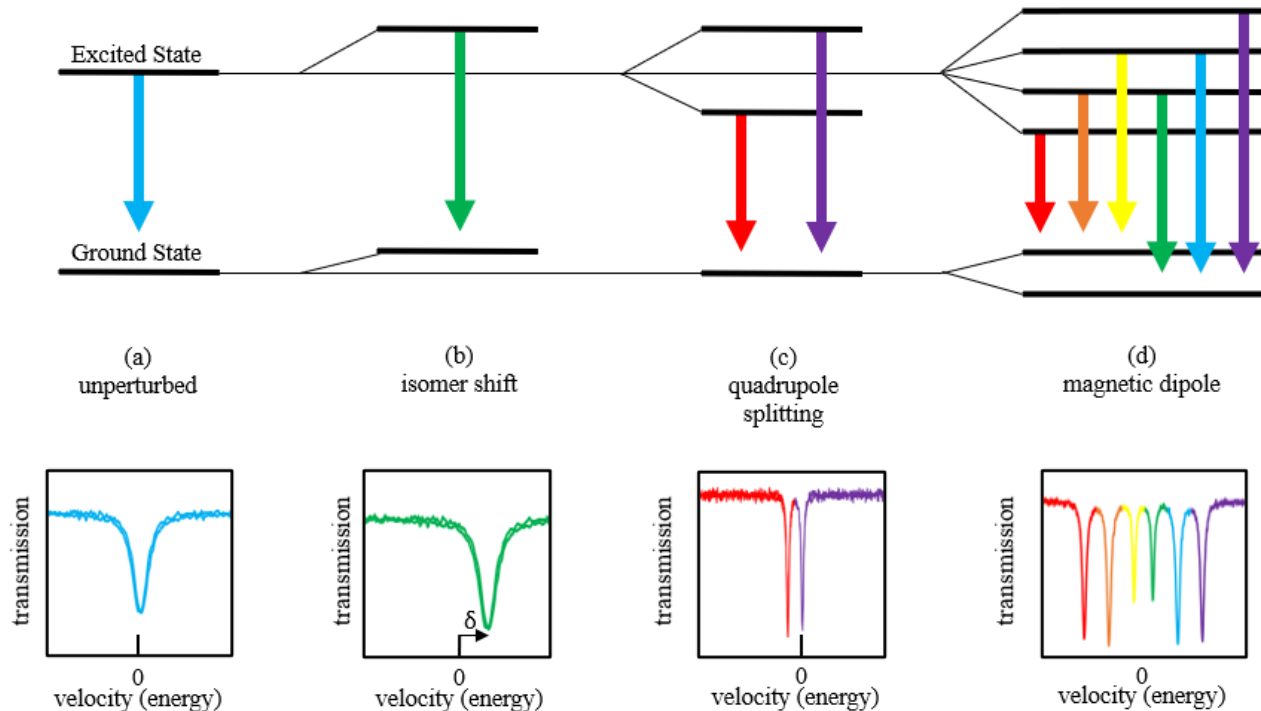


FIG. 2. Mössbauer spectrum of ^{57}Fe showing a) spectrum unperturbed with no hyperfine interactions seen, b) spectrum with only an isomer shift, c) spectrum with quadrupole splitting, and d) spectrum with magnetic dipole splitting. Image sourced and edited from Thomas [8].

becomes negligible when the atom is bound in a lattice. Additionally, Mössbauer found that recoil-less emission requires very small Doppler velocities, a few centimeters per second, because the atoms are held at approximately their equilibrium positions [2]. Atoms bound in a lattice are not perfectly rigid, so only a fraction of the γ -rays are resonantly absorbed. This relationship is described in the Lamb-Mössbauer fraction f as in Eq. 2.

$$f = e^{-k^2 \langle x^2 \rangle} \quad (2)$$

$\langle x^2 \rangle$ is the mean square displacement of the nucleus, and $k = \frac{2\pi}{\lambda}$ where λ is the wavelength of the γ -ray [4]. From this fraction it can be seen that only low energy γ -rays have the highest probability of detection in the Mössbauer spectroscopy.

The Mössbauer nuclei must have an excited state with very low energy, such that a recoil-less emission can occur, as well as a relatively long lifetime in order to get a good resolution. The probability of observing the Mössbauer effect also depends on temperature and the vibrational properties of the lattice. Stronger bonds and lower temperatures are more favorable [5]. While the Möss-

bauer effect was first detected using ^{192}Ir , it has been seen in many other isotopes. By far the most widely used due to its properties is ^{57}Fe [3, 6].

The Mössbauer spectroscopy can be used to study hyperfine interactions of atoms. The main three hyperfine interactions Mössbauer spectroscopy can study are

- electric monopole interactions,
- electric quadrupole interactions,
- magnetic dipole interactions,

as described in Ref. [8] and illustrated in Fig. 2.

An isomer shift, also known as the chemical shift, is the shifting of the entire resonance spectrum and is caused by the electric monopole interactions [2]. From the finite volume of the nucleus there is an electronic charge density for this volume. The charge density is affected by the finite electron volume and density. The electron density causes a shift in energy levels and the shift caused in the excited and ground states are different due to a difference in charge [6]. This shift is shown in Fig. 2b. The difference in separation between ground and excited states leads to a difference in shifting between absorber and source and this difference is the isomer shift δ . The

Doppler effect is used to detect the shift and the resonance line will be shifted by δ from zero velocity [6] as shown in Fig. 2. Since the isomer shift detects a shift between the absorber and the source, isomer shifts are determined from a standard absorber [2].

The electric quadrupole interactions are due to the electric field around the nucleus created by electrons and cause quadrupole splitting of spectral lines [2]. If an atom has a spin quantum number greater than $\frac{1}{2}$ its electron configuration cannot be considered spherical and instead is an asymmetric electric field [6]. This asymmetric electron density causes splitting of spectral lines as shown in Fig. 2c. In the case of ^{57}Fe it has a spin quantum number of $\frac{3}{2}$, the excited state is split between $m = \frac{1}{2}$ and $m = \frac{3}{2}$, where m is the magnetic spin number [4]. In a Mössbauer spectrum the peaks are separated by the same energy that the spectral lines are separated by. Quadrupole splitting can reflect information about valence electron configurations, and the bonding environment of the lattice [6].

In the case of electric quadrupole splitting we see a degeneracy in the magnetic spin number. This is shown in the case of ^{57}Fe where we would expect four spectral lines in the excited state, but only see two, so it is doubly degenerate [4]. This occurs because the energy levels are too close to each other [2]. When a magnetic field is applied the magnetic moment μ of the nucleus, caused by unpaired electrons, interacts with the applied magnetic field which makes the degeneracy apparent [6]. This effect is called Zeeman splitting and is shown in Fig. 2d.

After the spectral lines have experienced magnetic splitting, each transition between nuclear sub-states has a specific probability, depending on the angle between the direction of the magnetic field and the γ -ray. These probabilities are reflected proportionally in the intensity of the spectral lines. This can give us information about the orientation of the γ -ray beam to the magnetic field in our setup. In ^{57}Fe , there are six possible energy transitions between $I = \frac{1}{2}$ and $I = \frac{3}{2}$, such that the absorption peaks have relative intensities of 3:2:1:1:2:3, as shown in Fig. 2d [9].

II. DATA COLLECTION

We first collected data to calibrate the gas detector and make sure we could correctly select the γ emission from ^{57}Co at 14.4 keV. We used a proportional gas detector filled with 97% Krypton and 3% CO_2 at 760 Torr. The expected resolution was 5% FWHM 14.4 keV with a voltage setting of +1850 volts. The outer detector shell was stainless steel with a very thin (0.01 inch) beryllium

window with a 1 inch diameter. ^{57}Co emits γ -rays at 14.4 keV, 122 keV and 136 keV respectively with probability of 9%, 86% and 11% [7]. A spectrum of the γ emitted by our ^{57}Co source is shown in Fig. 4a.

We then adjusted the settings of the amplifier and shaping amplifier to minimize the FWHM of the 14.4 keV gamma peak for ^{57}Co . To do this we used the setup shown in Fig. 3. In this setup the drive unit and the absorber were not used, so the ^{57}Co source was not moving. The γ -rays were detected using the proportional counter [10] and the output signal from the detector was sent to a pre-amplifier (Wissel PEA6). The output of the pre-amplifier was then sent to an amplifier (NIM module, model ORTEC 590A [11]) for which we varied the gain settings from 5 to 50 using the dial on the module. The output of the amplifier was then sent to a shaping amplifier (NIM module model ORTEC 672 [12]). On the shaping amplifier we modified the gain settings from 5 to 50, and the shaping time from 0.5–10 μs . We tested the shaping times and gains with both a triangle and Gaussian shaping functions. The duration of each run lasted until the maximum of the peak corresponding to 14.4 keV was at least 5,000 counts. All peak data was collected and stored using the MAESTRO software [13]. The results are summarized in Tab. I.

TABLE I. Resolution obtained for the gamma peak at 5.9 keV and 14.4 keV with different settings of the shaping time and shaping time functions for the ORTEC 672 module.

672 Shap. T [μs]	Shap. Func.	5.9 keV FWHM[%]	14 keV FWHM[%]
0.5	Gauss	9.1	5.3
1	Gauss	8.9	5.0
2	Gauss	8.9	5.0
3	Gauss	7.9	4.6
6	Gauss	8.4	4.7
10	Gauss	—	5.1
0.5	Triangle	8.2	4.9
1	Triangle	7.8	4.8
2	Triangle	8.1	4.8
3	Triangle	7.5	4.8
6	Triangle	8.8	4.9
10	Triangle	—	5.8

To collect the absorption spectrum of ^{57}Fe , we connected the ^{57}Co source to the Wissel Mössbauer Drive System-360 [14], the source was produced in June 2023 with a nominal power of 25 mCi. The drive unit was set to have a maximum velocity of 12.026 ± 0.002 mm/s and a triangular function was used to drive the velocity unit with a 1024 steps. The distance between the absorber and drive unit was set to 20.6 mm and the distance between the absorber and the detector was 16.5 mm. The

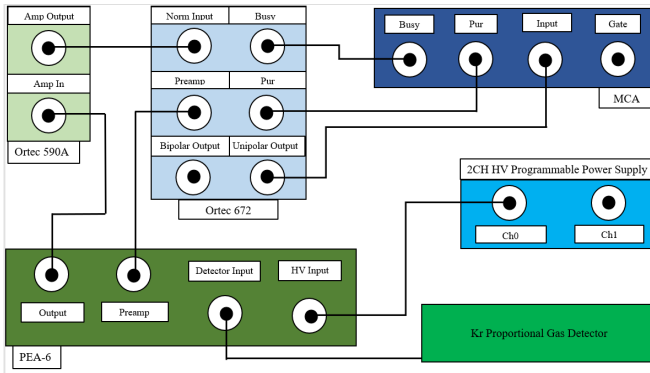


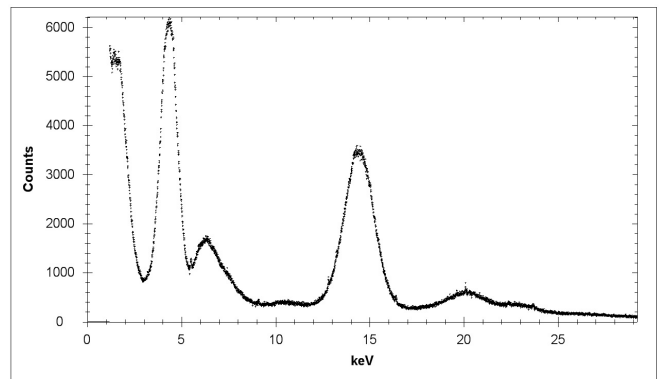
FIG. 3. Setup used to analyze the 14.4 keV gamma emission peak spectrum for the ^{57}Co source. Setup includes ORTEC 590A, ORTEC 672, Kr gas counter detector, pre-amplifier Wissel PEA-6, Multi Channel Analyzer, and a CAEN 2 Channels High Voltage Power Supply.

ORTEC 590A was set with a fine gain of 0.5 and a coarse gain of 10, while the ORTEC 672 uses a triangular shape function with shaping time of $0.5 \mu\text{s}$ and a coarse gain setting of 0.5. On the Wissel software the threshold was set between 2.1–2.8 Volts channels with a threshold of 98 mV.

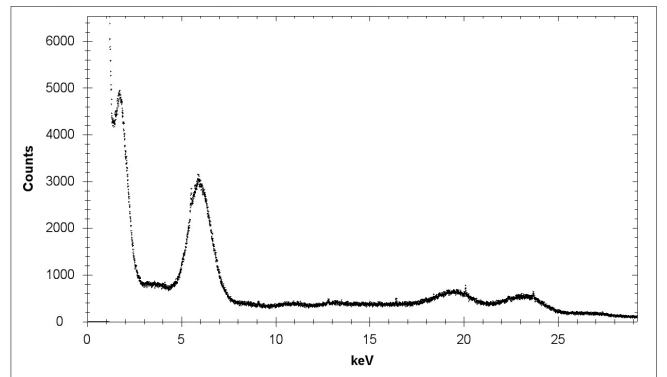
We collected data using 4 different absorbers: $\alpha\text{-Fe}$, Fe_2O_3 , $^{57}\text{FeC}_2\text{O}_4 \cdot 2\text{H}_2\text{O}$, and $\text{K}_2\text{Mg}^{57}\text{Fe}(\text{CN})_6$. The data collection lasted 1 and 3 hours respectively for each of the absorbers. The absorbers were placed in an holder and remained stationary. All data was collected using the Wissoft 2003 software [15]. We made sure that we collected data only for the 14.4 keV line using a discriminator threshold internal to the Multi Channel Analyzer. We set the threshold looking at the γ spectrum and we verified our energy scale using a ^{55}Fe source that emits γ -rays at 5.9 keV and ^{57}Co , which has a strong spectral line at 14.4 keV, as seen in Fig. 4.

III. DATA ANALYSIS

Data collected from different runs acquired using various settings for both the amplifier and shaping amplifier were analyzed using the TFit class in ROOT. We first graph the spectrum as function of channels and then apply a Gaussian fit function using ROOT and record both the mean and FWHM of the distributions. The fit function was applied within a specific range. We then plotted the FWHM vs. the tested parameter to find which gain, shaping time, and shaping type minimized our FWHM. We found the minimum FWHM to occur with minimum gain on both the ORTEC 590A and the ORTEC 672. We also found that FWHM is minimized approximately



(a) γ spectrum emitted by ^{57}Co and detected with a Kr gas detector. The graph shows a peak at 14.4 keV.

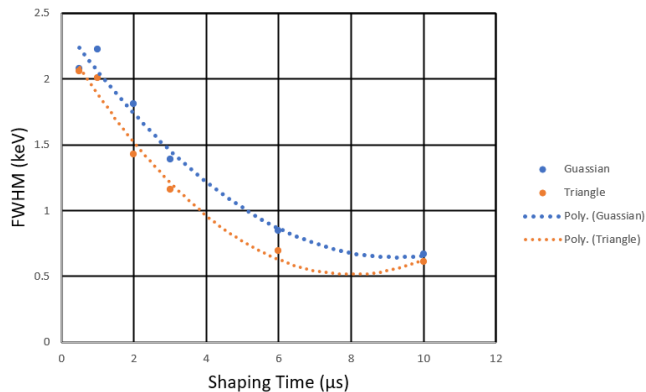


(b) γ spectrum emitted by ^{55}Fe and detected with a Kr gas detector. The graph shows a peak at 5.9 keV.

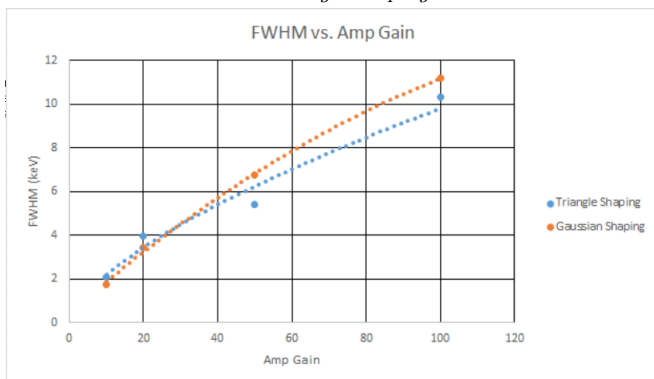
FIG. 4. Energy spectra taken using the Wissoft software.

around $10 \mu\text{s}$ shaping time. At greater shaping times greater than $3 \mu\text{s}$, however, the pile-up rejector turned on. These minimums are visualized in Fig. 5. Triangular shaping minimized the FWHM compared to Gaussian shaping for all gains and shaping times tested.

The absorption spectrum data is initially saved in the format of channels vs. count through the Wissoft software. Therefore, the first step in the analysis was to find the correlation between channel and velocity in mm/s using the settings of the drive unit. Our drive unit can accept different functions to drive the motor; in this study we used were a triangular wave. In the case of the triangular function, the rate of the change in the velocity is constant. The initial velocity starts and ends at 12.026 mm/s and reaches a minimum of -12.026 mm/s as shown in Fig. 6. Due to the constant rate of change of velocity everywhere except at the minimum, we were able to correlate the channels to velocity through a linear function. Additionally, because the drive unit passes through each velocity twice in one cycle every data point is duplicated. To resolve the mirrored data we took an equally weighted average of the duplicated data sets.



(a) FWHM changing with various shaping times for Gaussian and triangle shaping.



(b) FWHM changing with various gains on the ORTEC 590A for Gaussian and triangle shaping.

FIG. 5. FWHM data for various shaping times, shaping type and gain for the 14.4 keV peak of ^{57}Co .

Our absorption spectrum contains quadratic noise due to distortion and noise from the triangular function generator that drives the unit [16]. To estimate the noise we performed a quadratic fit to our data using Microsoft Excel's Data Analysis tools. We then subtracted the noise from our averaged data set.

To further analyze the absorption spectrum we fit each peak to a Lorentzian probability density function defined in Eq. 3.

$$F(x) = \frac{A}{1 + \left(\frac{x-x_0}{\sigma}\right)^2} \quad (3)$$

where A is the amplitude, σ is one standard deviation, and x_0 is the mean of a peak. The fit was used to find the peak positions and FWHM, for each peak in the absorption spectrum. We repeat the fit using algorithms developed for both Python [17] and ROOT [18]. In the case of the Python fit we assumed just a Lorentzian probability distribution function (PDF) while using ROOT we use

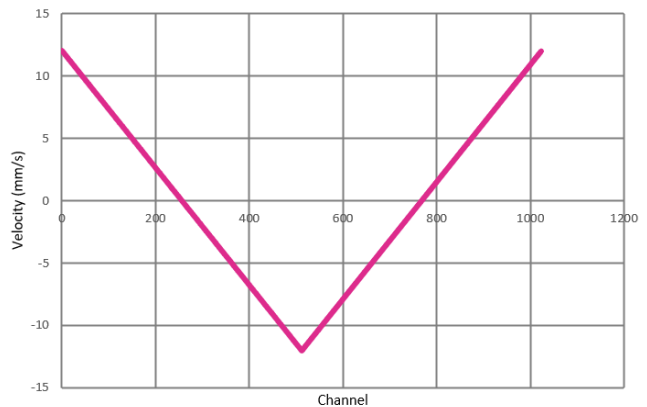


FIG. 6. Triangle drive shaping function as function of time. This graph shows the correlation between channel and velocity of the drive unit.

both a Gaussian and a Lorentzian. In both cases we fit the amplitude, the FWHM, and the mean peak positions for each peak in the absorption spectrum.

The data used for this fit was the averaged data set with the quadratic noise subtracted. The Lorentzian function was applied to each peak with orthogonal distance regression (ODR) using SciPy's ODR package. In order to use this package the data was inverted such that the minimums in the absorption spectrum became maximums. The fit was able to propagate the errors in both the x and y directions. The errors in the x-direction were assumed to be 0.5% of the velocity and uncorrelated bin to bin. The errors in the y-direction were assumed to be purely statistical $\frac{1}{\sqrt{\text{counts}}}$. The errors in x were derived from an integral of the error given by the motor drive unit. Errors in the drive unit are computed integrating in time the difference between the input signal and a feedback loop from the motor unit. The goodness of fit was determined evaluating the reduced χ^2 returned by the fit algorithm. Reduced χ^2 is defined as χ^2 divided by the number of degrees of freedom (n.d.o.f.).

Using the ROOT framework, we defined the Lorentzian fit as a customized function. We input the averaged data set for each bin after unfolding. We graphed the data using the TGraph package in ROOT and made a TFit variable for each peak in a given graph. The parameters were determined by automatically centering the peaks around the maximum values, and the width could be manually altered in order to achieve the best possible reduced χ^2 value. We repeated the same analysis also in Python.

To find the hyperfine interactions for each of our absorbers we first looked at the Zeeman splitting. The Zee-

man splitting energies g_0 and g_1 are the energy differences between sub-levels in the ground and excited states, respectively [19]. In order to determine these values, we took the weighted values of the differences between transitions that share either a ground state or an excited state [20].

The value of quadrupole splitting, denoted as ϵ , was found by comparing the values of the peak positions as in Eq. 4.

$$\begin{aligned}\Delta E_6 - \Delta E_5 &= g_1 + 2\epsilon \\ \Delta E_2 - \Delta E_1 &= g_1 - 2\epsilon.\end{aligned}\quad (4)$$

The isomer shift δ is the weighted average of the absorption peak centers.

After propagating errors, we compared these values to those from a reference absorber. The difference between the expected and experimental values determines the goodness and systematic uncertainties in the correspondence between channel and velocity.

TABLE II. *Minimum and maximum reduced χ^2 values for both Python and ROOT fitting procedures during a three hours acquisition time.*

Absorbers		$\chi^2/ndof$
α -Fe	Python	10.7-23.6
	ROOT	3.7-25
Fe ₂ O ₃	Python	1.8-3.6
	ROOT	0.91-5.7
⁵⁷ FeC ₂ O ₄ ·2H ₂ O	Python	15.0-21.6
	ROOT	0.96-1270
K ₂ Mg ⁵⁷ Fe(CN) ₆	Python	5.7
	ROOT	409

IV. RESULTS

In the case of the Python fit the reduced χ^2 varied from 0.6 to 23.6 as summarized in Tab. II.

The fit for the α -Fe was run on a three hours absorption spectrum has shown in Figs. 7 and 8. All others spectra are presented in Appendix VII. All of our fit results are summarized in Tab. III.

For the Python fit we found that the reduced χ^2 was consistently larger in the case of the spectrum acquired with 3 hour runs than for the 1 hour runs. We also found that the values of the χ^2 for the two central peaks in the absorption spectrum (peak 3 and 4), were greater than the other peaks for α -Fe and Fe₂O₃.

TABLE III. *Python analysis of an α -Fe absorber acquired with a three hours running time. The mean, FWHM, amplitude and reduced $\chi^2/n.d.o.f.$ are shown for each absorption peaks.*

Peak	Mean	FWHM	Ampl.	$\chi^2/n.d.o.f.$
1	-5.460±0.001	0.483±0.004	28,082±114	14.4
2	-3.235±0.001	0.516±0.004	29,698±104	10.7
3	-0.972±0.001	0.356±0.003	20,398±91	15.1
4	0.746±0.001	0.365±0.003	20,282±93	23.6
5	3.018±0.001	0.520±0.004	29,541±111	12.9
6	5.247±0.001	0.480±0.004	28,117±92	11.5

TABLE IV. *ROOT analysis of an α -Fe absorber acquired with a three hours running time. The mean, FWHM, amplitude and reduced $\chi^2/n.d.o.f.$ are shown for each absorption peaks.*

Peak	Mean	FWHM	Ampl.	$\chi^2/n.d.o.f.$
1	-5.466±0.006	0.824±0.01	14,996±254	1.37
2	-3.231±0.003	0.923±0.01	17,547±224	1.60
3	-0.965±0.001	0.604±0.006	7,771±60	24.9
4	0.747±0.001	0.612±0.003	7,615±29	16.3
5	3.020±0.003	0.925±0.01	17,411±213	1.41
6	5.250±0.004	0.801±0.02	14,968±252	1.17

We checked the means found for α -Fe with RITVERC's test report for α -Fe and found that the values agree within the tenths place [21].

In the case of the ROOT analysis, our reduced χ^2 varied from a minimum of 0.912 to 1270. For α -Fe, we got reduced χ^2 values from 1.53 to 39.3 in the one hour run and 1.17 to 24.9 in the three hour run.

When analyzing Fe₂O₃, we observed that the χ^2 values varied from 1.02 to 7.11 for the one hour run and between 0.91 to 5.68 for the three hour run. In both of these absorbers, the fit improved in longer runs when the statistical error was less, and the fit produced larger reduced χ^2 values for the middle peaks (3 and 4).

The absorption spectrum for the K₂Mg⁵⁷Fe(CN)₆ only had one peak, with a reduced χ^2 value of 119 during the one hour run and 409 in the three hour run. The absorption spectrum for the ⁵⁷FeC₂O₄·2H₂O had two peaks. The first peak varied from χ^2 values of 925 to 1270 between the two runs, whereas the second peak had much smaller values of the χ^2 between 1.03 to 0.96. For both of these absorbers, the reduced χ^2 values were extremely high and increased for longer runs.

The α -Fe spectrum acquired for three hours is shown in Fig. 8 and the value of the fit parameters and χ^2 are shown in Tab. IV. We have added errors in both x and y. As mentioned before the errors in y are the simple statistical error on the sample collected after the quadratic

noise subtraction. The error in x are the error on the velocity vs channel and they are computed using the feedback loop on the Wissel driver unit. All other absorption spectrums and fit results are reported in Appendix VII.

The known value of the isomer shift for α -Fe is measured as -0.109 mm/s by RITVERC, which is within the error bounds of the value we calculated during the three hour run using ROOT [21, 22].

We were unable to compare values for Fe_2O_3 to a RITVERC reference sheet because the sheet provided only lists the isomer shift relative to $\text{Co}(\text{Rh})$. Instead, we found an outside source to provide ϵ and δ values for Fe_2O_3 [23, 24].

For $^{57}\text{FeC}_2\text{O}_4 \cdot 2\text{H}_2\text{O}$, the given spectrum parameters are the isomer shift relative to α -Fe and the quadrupole splitting, which we found with errors of 0.065 and 0.484, respectively [25].

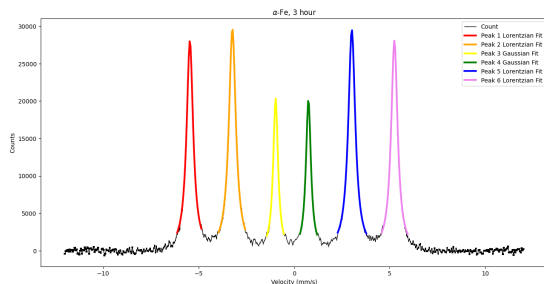


FIG. 7. Python analysis of an α -Fe acquired with a three hours running time. Each peak is individually fit with a Lorentzian probability distribution using orthogonal distance regression (*scipy.odr*).

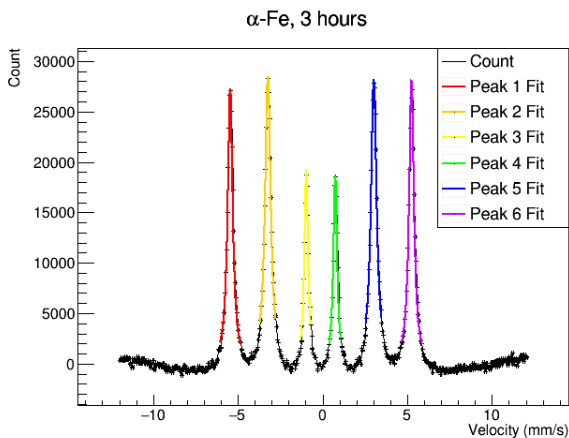


FIG. 8. ROOT analysis of an α -Fe acquired with a three hours running time. Each peak is individually fit with a Lorentzian probability distribution using the *TF1* class with an internally defined function.

$\text{K}_2\text{Mg}^{57}\text{Fe}(\text{CN})_6$ had the largest error in the isomer shift, possibly because there was only one peak to analyze. The closest isomer shift we found was 0.99 times greater than the expected value [26].

We found that Python had a isomer shift (δ) within 0.1% of the expected value in α -Fe, outperforming ROOT. However, ROOT had a maximum δ error of 12.1% in Fe_2O_3 , which was more accurate than Python for the same absorber.

The $^{57}\text{FeC}_2\text{O}_4 \cdot 2\text{H}_2\text{O}$ and $\text{K}_2\text{Mg}^{57}\text{Fe}(\text{CN})_6$ had roughly similar values for both fitting procedures. $\text{K}_2\text{Mg}^{57}\text{Fe}(\text{CN})_6$ in particular had a very large error for both programs. We posit that this is due to the single peak, which means that we cannot take multiple measurements to find the weighted average.

ϵ (quadrupole splitting) errors were roughly the same for both fitting procedures, and the data does not definitively suggest that one procedure is more accurate than the other.

V. CONCLUSION

To minimize the FWHM of the 14.4 keV for ^{57}Co we recommend using a gain of 5 for both the amplifier (ORTEC 590A) and the shaping amplifier (ORTEC 672). We also recommend using a shaping time of 3 μs with a triangular shaping function. We do not recommend going above 3 μs for the shaping time due to the pile-up increasing significantly for shaping times greater than 3 μs .

When the Zeeman effect is present in the absorber spectrum, we found that ROOT consistently had a better goodness of fit for peaks 1, 2, 5, and 6, but Python fit the inner peaks, peaks 3 and 4, with a better goodness of fit. Despite that, peaks 3 and 4 still had the largest reduced χ^2 with respect to any of the other peaks. We believe the inner peaks consistently had the largest reduced χ^2 because they are a superposition of both Gaussian and Lorentzian distributions. We wish to test this hypothesis with further testing by fitting the peaks with Gaussian and Lorentzian probability density functions.

When Zeeman effects is not present in the absorber spectrum, we found that the reduced χ^2 for the Python fits were consistent with reduced χ^2 when Zeeman effects are present, as seen in Fig. 9.

ROOT was less consistent and had very large reduced χ^2 values for the $^{57}\text{FeC}_2\text{O}_4 \cdot 2\text{H}_2\text{O}$ and the $\text{K}_2\text{Mg}^{57}\text{Fe}(\text{CN})_6$ absorbers. Due to the inconsistency seen with ROOT for fits with no Zeeman effect, we recommend using the Python fit when no Zeeman effect is

TABLE V. g_0 in meV, g_1 in meV, ϵ in mm/s and δ in mm/s. Values obtained using Python fitting procedure for each of the absorbers for different acquisition time.

Absorbers		g_0 [meV]	g_1 [meV]	ϵ [mm/s]	δ [mm/s]
α -Fe	Python	1.92 ± 0.01	1.08 ± 0.01	$(-1.21 \pm 0.08) \times 10^{-2}$	-0.109 ± 0.004
	ROOT	1.92 ± 0.01	1.08 ± 0.01	$(-8.07 \pm 2) \times 10^{-3}$	-0.104 ± 0.004
	Theo.	—	—	—	$[-0.1090 \pm 0.0001]$
Fe ₂ O ₃	Python	2.96 ± 0.02	1.67 ± 0.02	-0.105 ± 0.007	0.284 ± 0.004
	ROOT	2.96 ± 0.02	1.67 ± 0.02	-0.106 ± 0.007	0.252 ± 0.004
	Theo.	—	—	$[-0.1000 \pm 0.0005]$	$[0.24 \pm 0.04]$
⁵⁷ FeC ₂ O ₄ ·2H ₂ O	Python	—	—	0.881 ± 0.001	1.11 ± 0.004
	ROOT	—	—	(0.887 ± 0.001)	1.11 ± 0.004
	Theo.	—	—	$[1.72 \pm 0.84]$	$[1.19 \pm 0.07]$
K ₂ Mg ⁵⁷ Fe(CN) ₆	Python	—	—	—	-0.216 ± 0.004
	ROOT	—	—	—	-0.201 ± 0.004
	Theo.	—	—	—	$[-0.10 \pm 0.12]$

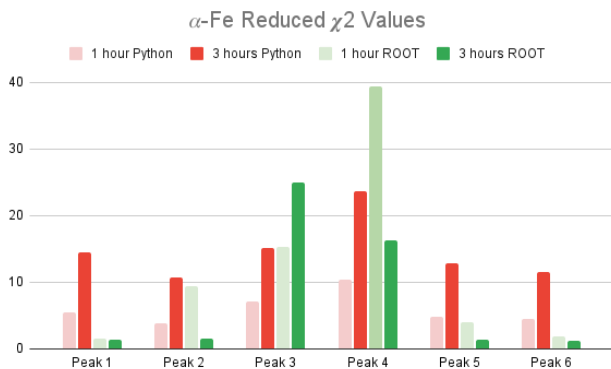


FIG. 9. Comparison of reduced chi-squared for α -Fe absorber runs for 1 and 3 hours. Red bars are the Python fit reduced chi-squared and green bars are the ROOT reduced chi-squared.

present.

A consideration for the Python fit is the unexpected increase of the reduced χ^2 with the longer run times. It was expected with longer run times the overall number of counts to increase, and thus decrease the expected error percentage associated with the counts. The decrease in error associated with the data should have created a better goodness of fit, but in Python it consistently created a larger reduced χ^2 . In ROOT, however, we see the expected decrease in the reduced χ^2 for absorbers with no Zeeman effect (Fig. 8).

While Python calculated slightly more accurate Mössbauer spectroscopy parameters in the case of α -Fe, ROOT still predicted the correct value within the error bounds, and in other absorbers it performed the same or significantly better. In the future, we would like to compare this data to predicted Zeeman effect parameters in order to see which program is better at calculating those.

Overall, we recommend using a gain of 5 on the ORTEC 590A and 672, shaping time of 3 μ s, and triangular shaping for the ORTEC 672. We also recommend using the ROOT fit when a Zeeman effect is present, but to use the Python fit when no Zeeman effect is present. Both fits were able to accurately find the mean of each peak to perform calculations on finding the hyperfine interactions present.

VI. ACKNOWLEDGEMENTS

We would like to thank our mentor, Prof. Camillo Mariani, Dr. Matt Murphy, and Mr. Dipanjan Mitra for their help and guidance.

We acknowledge the outstanding support from the National Science Foundation, the Virginia Tech Physics Department and the Virginia Tech Center for Neutrino Physics. This work was made possible by the National Science Foundation under grant No. PHY-2149165.

-
- [1] Mössbauer, R.L. Kernresonanzfluoreszenz von Gammas-
trahlung in Ir191 . Z. Physik 151, 124–143 (1958).
<https://doi.org/10.1007/BF01344210>
- [2] Y.L. Chen J and D.P. Yang, *Mössbauer Effect in Lattice
Dynamics* (2007).
- [3] H. Frauenfelder, *The Mössbauer Effect* W. A. Benjamin,
Inc., New York, 1962.
- [4] T.E. Cranshaw, *Mössbauer Spectroscopy*, Journal of
Physics E: Scientific Instruments 7, (1974).
- [5] Preston, R. S., Hanna, S. S. and Heberle, J. (1962)
"Mössbauer Effect In Metallic Iron*", Phys. Rev. 128,
2207-2218.
- [6] D.P.E. Dickson and F.J. Berry, editors *Mössbauer Spec-
troscopy* (Cambridge University Press, 1986).
- [7] Stanford Environmental Health and Safety, Radionuclide
Safety Data Sheet Radionuclide: Co-57 Forms: Soluble
Physical Characteristics, 2020.
- [8] Thomas, Sylvia-Monique. "Mössbauer Spectroscopy."
Mineral Physics, 17 Dec. 2022.
- [9] R.L. Cohen, *Applications of Mössbauer Spectroscopy*, Vol
1 (Academics Press, Inc., New York, 1976).
- [10] LND, Designers & Manufacturers of Nuclear Radiation
Detectors, 03 Mar. 2022
- [11] Model 590A Amplifier and Single-Channel Analyzer Op-
erating and Service Manual, Advanced measurement
Technology, Inc., 2002
- [12] Model 672 Spectroscopy Amplifier Operating and Service
Manual, 2002
- [13] MAESTRO, Advanced measurement Technology Inc.,
2012
- [14] MÖSSBAUER DRIVE SYSTEM 360 Instruction Man-
ual, Wissenschaftliche Elektronik GMBH, second edition
2.6
- [15] Data Acquisition Module CMCA-550 Instruction Man-
ual, Wissenschaftliche Elektronik GMBH, edition 2.2,
2004
- [16] Methods of Experimental Physics
(MXP) - Mössbauer Data,
[https://sites.google.com/a/umn.edu/mxp/advanced-
labs/mossbauer-effect-lab/mossbauer-data](https://sites.google.com/a/umn.edu/mxp/advanced-labs/mossbauer-effect-lab/mossbauer-data).
- [17] Van Rossum, G. & Drake, F.L., 2009. Python 3 Reference
Manual, Scotts Valley, CA: CreateSpace.
- [18] Rene Brun and Fons Rademakers, ROOT - An Ob-
ject Oriented Data Analysis Framework, Proceedings AL-
HENP'96 Workshop, Lausanne, Sep. 1996, Nucl. Inst.
& Meth. in Phys. Res. A 389 (1997) 81-86. See also
"ROOT" [software], Release 6.28/04, 08/05/2023
- [19] Science Engineering & Education Co., SEE Co Model
MS6S Student Lab Mössbauer Spectroscopy System User
Manual, 2014.
- [20] D. V. Perepelitsa, Mössbauer Spectroscopy of 57-Fe, MIT
Department of Physics, 2007.
- [21] RITVERC JSC, Test Report # 1168-2023, 2023.
- [22] RITVERC JSC, Mössbauer Reference Absorber
MRA.1.6, 2023.
- [23] RITVERC JSC, Mössbauer Reference Absorber
MRA.1.3.5, 2023.
- [24] Šepelák, V. & Isfahani, Mohammad & Ghafari, Mar-
jan & Feldhoff, Armin & Becker, K.. (2011). Com-
plementary 57-Fe and 119-Sn Mössbauer study of
mechanochemical redox reaction. Hyperfine Interactions.
202. 10.1007/s10751-011-0358-9.
- [25] RITVERC JSC, Mössbauer Reference Absorber
MRA.1.2.4, 2023.
- [26] RITVERC JSC, Mössbauer Reference Absorber
MRA.1.1.4, 2023.

VII. APPENDIX

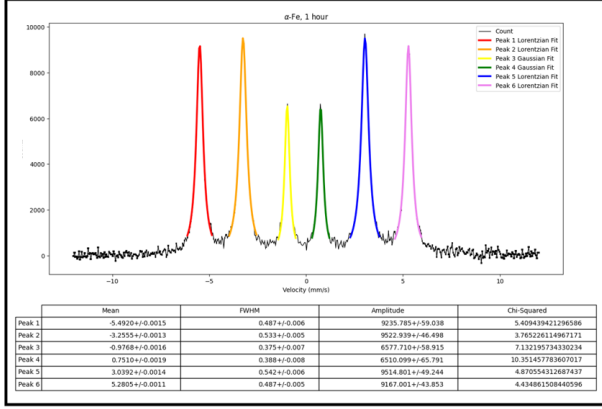


FIG. 10. Python analysis of an α -Fe absorber run for one hour. Each peak is individually fit with a Lorentzian probability distribution using orthogonal distance regression (*scipy.odr*). Below the graph the mean, FWHM, amplitude and reduced chi-squared is provided for each fit.

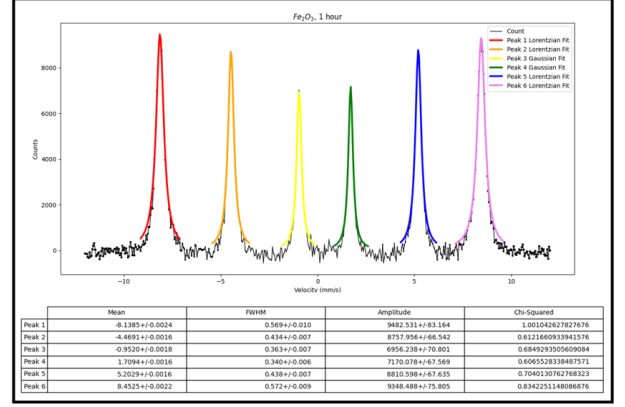


FIG. 11. Python analysis of a Fe_2O_3 absorber run for one hour. Each peak is individually fit with a Lorentzian probability distribution using orthogonal distance regression (*scipy.odr*). Below the graph the mean, FWHM, amplitude and reduced chi-squared is provided for each fit.

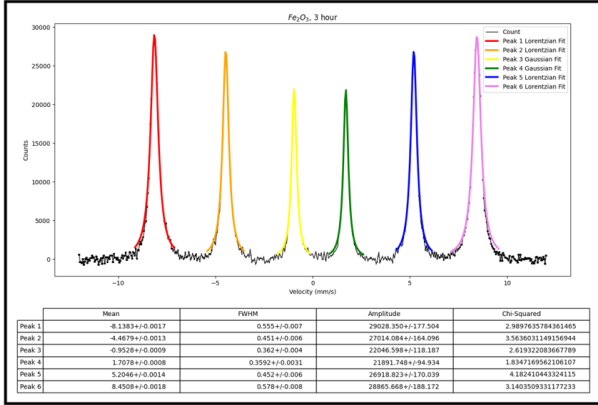


FIG. 12. Python analysis of a Fe_2O_3 absorber run for three hours. Each peak is individually fit with a Lorentzian probability distribution using orthogonal distance regression (*scipy.odr*). Below the graph the mean, FWHM, amplitude and reduced chi-squared is provided for each fit.

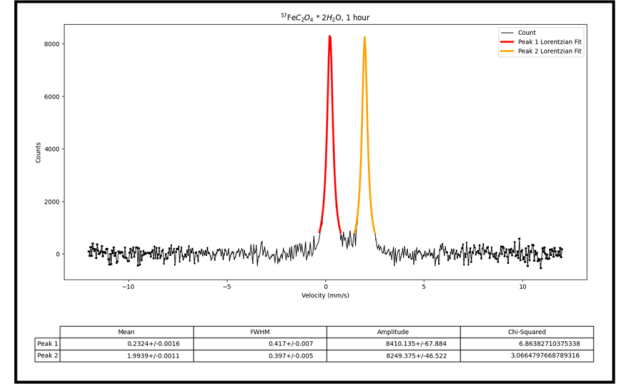


FIG. 13. Python analysis of a $^{57}FeC_2O_4 \cdot 2H_2O$ absorber run for one hour. Each peak is individually fit with a Lorentzian probability distribution using orthogonal distance regression (*scipy.odr*). Below the graph the mean, FWHM, amplitude and reduced chi-squared is provided for each fit.

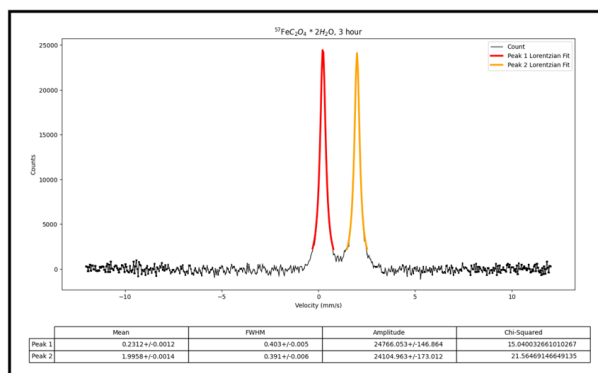


FIG. 14. Python analysis of a $K_2Mg^{57}Fe(CN)_6$ absorber run for three hours. Each peak is individually fit with a Lorentzian probability distribution using orthogonal distance regression (*scipy.odr*). Below the graph the mean, FWHM, amplitude and reduced chi-squared is provided for each fit.

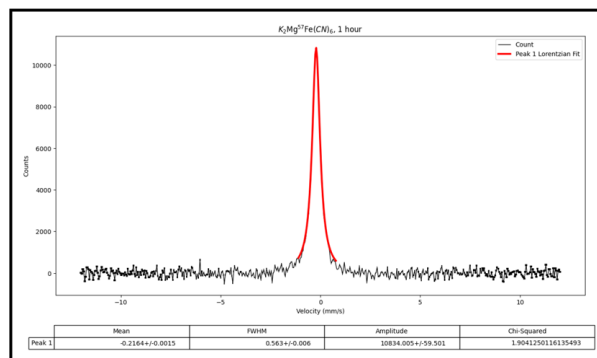


FIG. 15. Python analysis of a $^{57}FeC_2O_4 \cdot 2H_2O$ absorber run for one hour. Each peak is individually fit with a Lorentzian probability distribution using orthogonal distance regression (*scipy.odr*). Below the graph the mean, FWHM, amplitude and reduced chi-squared is provided.

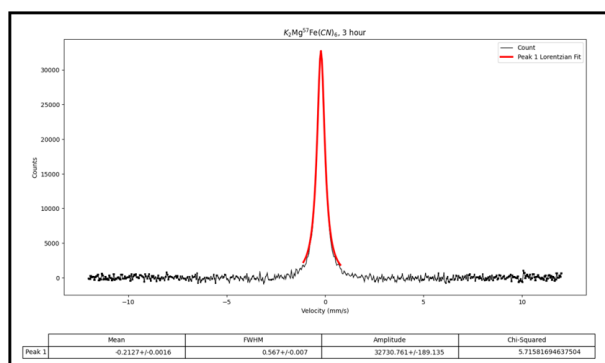


FIG. 16. Python analysis of a $^{57}FeC_2O_4 \cdot 2H_2O$ absorber run for three hours. Each peak is individually fit with a Lorentzian probability distribution using orthogonal distance regression (*scipy.odr*). Below the graph the mean, FWHM, amplitude and reduced chi-squared is provided.

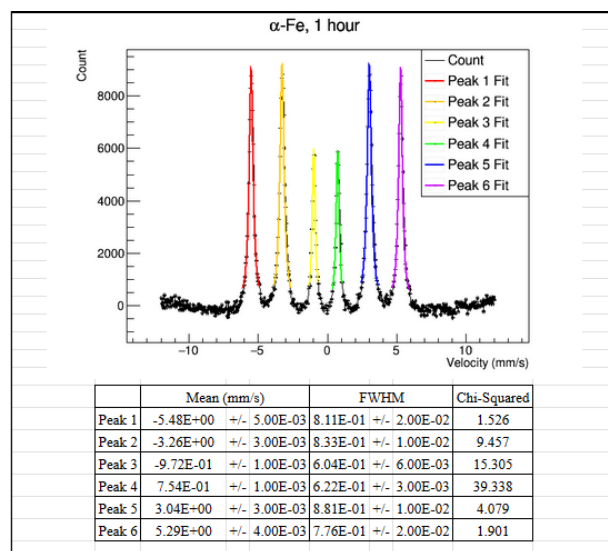


FIG. 17. ROOT analysis of an α -Fe absorber run for one hour. Each peak is individually fit with a Lorentzian probability distribution using *TFit*. Below the graph the mean, FWHM, and reduced chi-squared is provided for each fit.

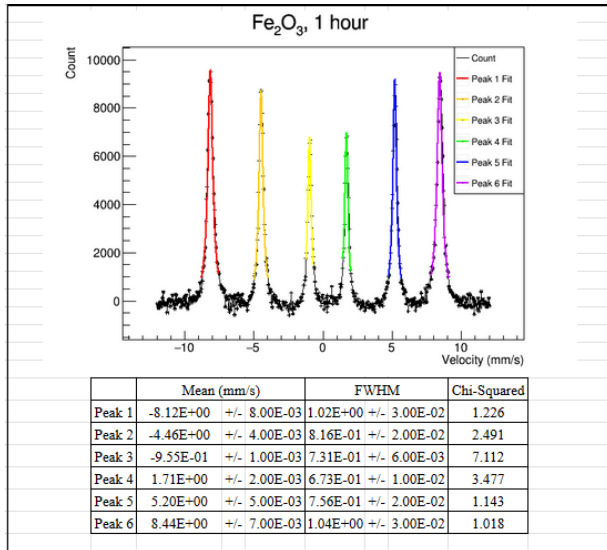


FIG. 18. ROOT analysis of an Fe_2O_3 absorber run for one hour. Each peak is individually fit with a Lorentzian probability distribution using TFit. Below the graph the mean, FWHM, and reduced chi-squared is provided for each fit.

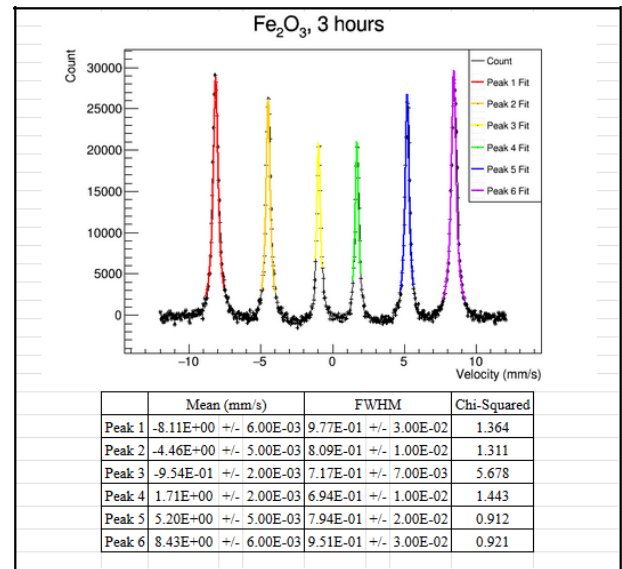


FIG. 19. ROOT analysis of an Fe_2O_3 absorber run for three hours. Each peak is individually fit with a Lorentzian probability distribution using TFit. Below the graph the mean, FWHM, and reduced chi-squared is provided for each fit.

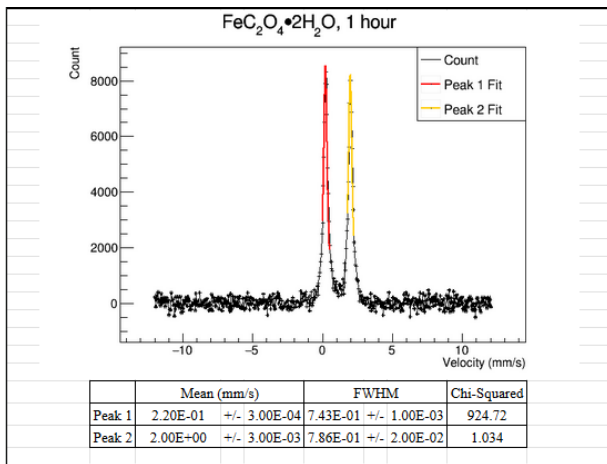


FIG. 20. ROOT analysis of an $\text{FeC}_2\text{O}_4 \cdot 2\text{H}_2\text{O}$ absorber run for one hour. Each peak is individually fit with a Lorentzian probability distribution using TFit. Below the graph the mean, FWHM, and reduced chi-squared is provided for each fit.

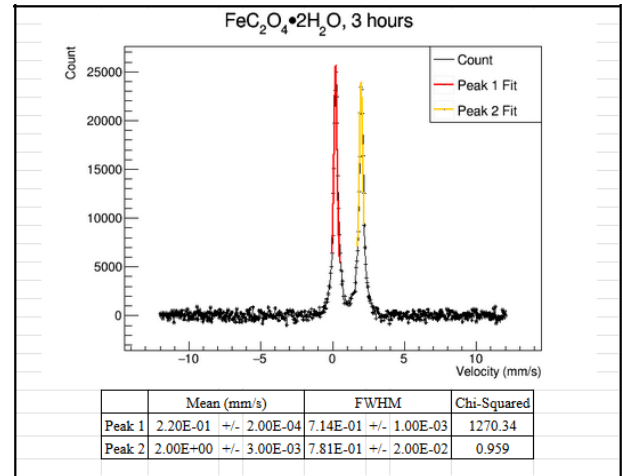


FIG. 21. ROOT analysis of an $\text{FeC}_2\text{O}_4 \cdot 2\text{H}_2\text{O}$ absorber run for three hours. Each peak is individually fit with a Lorentzian probability distribution using TFit. Below the graph the mean, FWHM, and reduced chi-squared is provided for each fit.

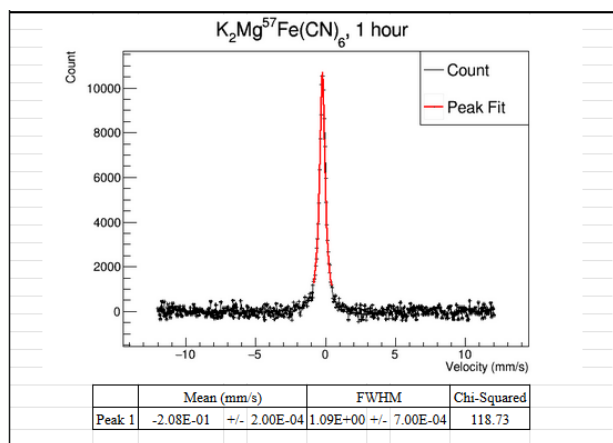


FIG. 22. ROOT analysis of a $K_2Mg^{57}Fe(CN)_6$ absorber run for one hour. Each peak is individually fit with a Lorentzian probability distribution using TFit. Below the graph the mean, FWHM, and reduced chi-squared is provided.

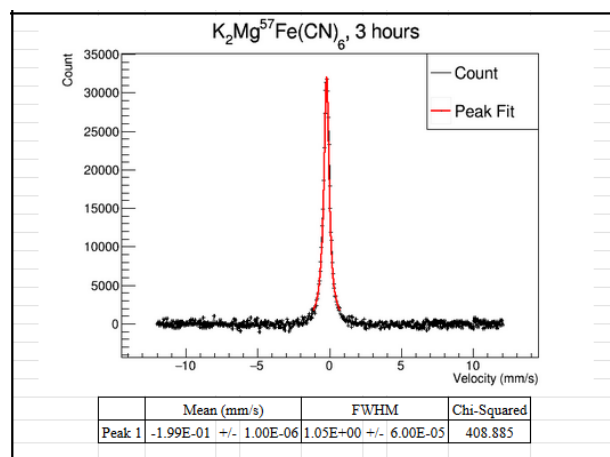


FIG. 23. ROOT analysis of a $K_2Mg^{57}Fe(CN)_6$ absorber run for three hours. Each peak is individually fit with a Lorentzian probability distribution using TFit. Below the graph the mean, FWHM, and reduced chi-squared is provided.

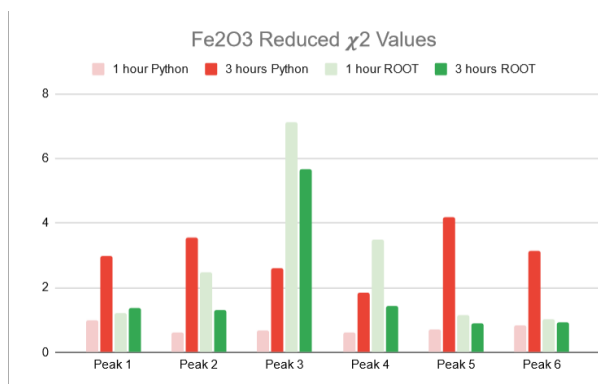


FIG. 24. χ^2 values for Fe_2O_3 in both ROOT and Python for both lengths of data collection.

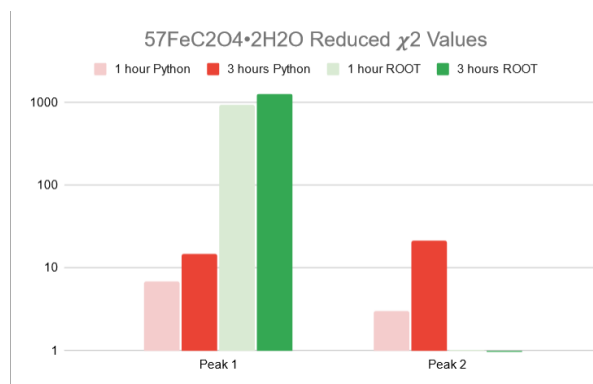


FIG. 25. χ^2 values for $^{57}FeC_2O_4 \cdot 2H_2O$ in both ROOT and Python for both lengths of data collection.

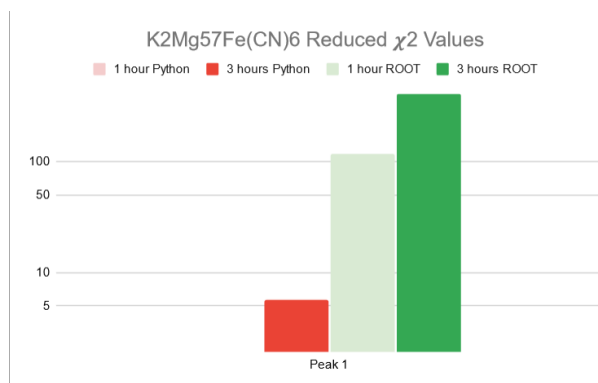


FIG. 26. χ^2 values for $K_2Mg^{57}Fe(CN)_6$ in both ROOT and Python for both lengths of data collection.